Int. J. Solids Structures Vol. 29, No. 20, pp. 2563–2582, 1992
Printed in Great Britain.

0020–7683/92 $5.00 + .00

RHEOLOGICAL MODELING OF CERAMIC COMPOSITES: AN INDIRECT METHOD OF INTERFACIAL MECHANICAL PROPERTY MEASUREMENTS

DALLAS W. MEYER†
Department of Engineering Mechanics and Engines Research Center, University of Wisconsin, Madison, WI 53706, U.S.A.

REID F. COOPER
Department of Materials Science & Engineering and Engines Research Center, University of Wisconsin, Madison, WI 53706, U.S.A.

and

MICHAEL E. PLESHA
Department of Engineering Mechanics, University of Wisconsin, Madison, WI 53706, U.S.A.

(*Received* 10 *January* 1991; *in revised form* 6 *January* 1992)

Abstract—A decomposition of the displacement and stress fields of a ceramic composite specimen subjected to an "off-axis" compressive loading allows the simulation of creep and load relaxation by integrating a generalized two-dimensional boundary value problem in time. A continuum approach is used for the composite model, with the matrix and fiber being described by nonlinear Maxwell fluid constitutive relations. The fiber matrix interface is described as an infinitely thin layer, in which a Coulomb friction constitutive model is used for the traction displacement response. This paper describes a fundamentally based micromechanical model in conjunction with several tools required for its solution, including an incremental plasticity formulation and a singular yield surface provision that utilizes proportional stressing. The resulting solution predicts the existence of a steady-state creep rate for the composite, which is a function of the fiber orientation angle, the stress exponent and the friction coefficient of the fiber matrix interface. Several conclusions are presented concerning the ability of this methodology to assess the rheologic response and interfacial mechanical behavior of ceramic composites at elevated temperatures.

1. INTRODUCTION

The room temperature behavior of the fiber–matrix interface during inelastic deformations of ceramic composites has been studied analytically by Aveston *et al.* (1971) (ACK theory), Budiansky *et al.* (1986), Aboudi (1989), Evans *et al.* (1989), Achenbach and Zhu (1989) and others. Micromechanical measurement techniques, such as the fiber indentation test [see e.g. Marshall and Oliver (1987)] have provided some limited quantitative information regarding interfacial behavior. Measurement of the fracture properties through bulk composite deformation and a statistical correlation to interfacial properties has been introduced by Thouless *et al.* (1989). One drawback of these measurement techniques is the experimental errors introduced by residual stresses, test specimen geometry and free surface effects, fiber breakage, etc.

Interface effects on the creep of metal matrix composites have been examined by Dragone and Nix (1990), Goto and McLean (1991), Brokenbrough *et al.* (1991), Evans *et al.* (1990) and others. The primary objective of these models is to predict the bulk composite behavior based upon constitutive models of the matrix and interface. We are considering the antithesis of this approach for the application to ceramic composites. Specifically, the premise of the present work is to analytically examine the role of interface deformations in the bulk creep/load relaxation response of a ceramic composite subjected to an off-axis compressional loading. We then use this information to predict the interfacial behavior of the composite.

†Currently at IBM Systems Storage Product Division, Rochester, MN 55901, U.S.A.

The model developed for this purpose is summarized and discussed relative to using the ideas for quantifying the interfacial mechanical behavior during high temperature deformation. The predictions of the model are compared to experimental results obtained on a ceramic composite system where a calcium aluminosilicate matrix is reinforced with continuous silicon carbide fibers (Chyung *et al.*, 1986): the experimental results are described fully in Meyer *et al.* (1992a).

The generality of the composite rheology model has been maintained in the interest of extending these ideas to other materials and geometries. The two constitutive models being used to illustrate the method for ceramic composites are a nonlinear Maxwell fluid for the continuum elements of the composite (fiber and matrix), and a Coulomb friction idealization for the fiber–matrix interface. The solution of the incremental boundary value problem which incorporates these features has required the use of several analytical tools, including a non-Newtonian bulk rheology in three-dimensions and a penalty method coupled with an incremental plasticity formulation to account for the contact friction at the interface. In addition, several developments were required to solve the composite problem, including a deformation theory for solving the problem of a singular yield surface and several numerical procedures including a specialized time integration scheme [the numerical developments are fully described in Mayer *et al.* (1992b)]. These features will be illustrated in the following developments, after which the results and implications for the composite problem will be discussed.

2. GENERAL APPROACH TO THE COMPOSITE MODEL

In order to correlate the mechanical response of the interface to the bulk composite response, the concept of equivalent homogeneity will be used (Christensen, 1979) to describe the composite stress and deformation at two distinct lengthscales, the mesoscale and the microscale. The mesoscale, with a length scale of the order of 10 fiber diameters, remains measurably small with respect to the characteristic dimensions of the sample. The microscale, then, considers the stress and deformation fields associated with a length scale of the order of a single fiber; it is, however, sufficiently large such that the continuum hypothesis is rational. In this work, the mesoscale is subdivided into some characteristic unit of representation, specifically the microscale, on which the stress and deformation analyses are completed; the unit results are then redefined in terms of the mesoscale.

The equivalent homogeneity concept is used to model the effect(s) of varying the fiber orientation angle (relative to the applied compressive load) of a unidirectional, continuous fiber-reinforced ceramic composite subjected to a compressive mesoscale stress at elevated temperatures, as illustrated in Fig. 1(a). Several assumptions concerning the mesoscale and

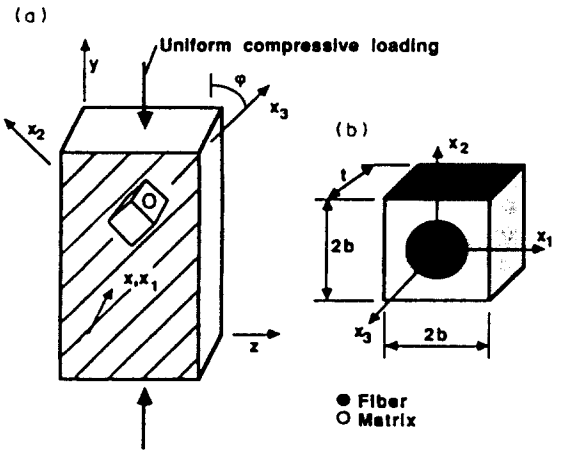

Fig. 1. Off-axis decomposition: (a) Compression specimen with the applied compressive loading (σ_{yy}). (b) Unit-cell microscale model. The coordinate systems are shown corresponding to the specimen (x, y, z) and the microscale model (x_1, x_2, x_3).

microscale stress and deformation fields are required in order to employ a two-dimensional analysis. The first assumption is that the mesoscale stress field is homogeneous: unconstrained translation and/or rotation of the compression specimen ends is permitted. This assumption allows the microscale analysis to be done on an isolated single fiber, or on a small group of fibers, at some arbitrary point along its (their) length, since the mesoscale fields do not vary in the fiber direction. A microscale assumption, then, is that the composite can be represented as two isotropic, distinct materials, the fiber and the matrix, separated by an infinitesimally thin interface.

The assumption of a single unit-cell model as a characteristic unit of representation is taken in this discussion [see Fig. 1(b)], however the ideas developed here could be used on any geometrically consistent group of fibers [see e.g. Brokenbrough *et al.* (1991)]. With this in mind, the developments that follow will retain a certain degree of generality, thus allowing for the possibility of differing geometrical models.

Considering the microscale analysis of Fig. 1(b) (without loss of generality, set the thickness t equal to unity), a separation of in-plane and out-of-plane deformations is assumed,

$$u_1 = u_1(x_1, x_2), \quad u_2 = u_2(x_1, x_2), \quad u_3 = \bar{u}_3(x_1, x_2) + x_3\varepsilon_{33}, \tag{1}$$

where u_i are displacements and the out-of-plane strain, ε_{33}, is not a function of the spatial coordinates. Compatibility requirements for the mesoscale, along with the symmetry conditions apparent in Fig. 1(b), can be stated as

$$u_1(\pm b, x_2) = \pm u_1^c, \quad u_2(x_1, \pm b) = \pm u_2^c, \quad \bar{u}_3(x_1, \pm b) = \pm u_3^c, \tag{2}$$

where the u_i^cs are constants. Equilibrium will be satisfied between the mesoscale and microscale stress fields in an average sense, by transforming the average mesoscale stress to a coordinate system corresponding to the fiber orientation:

$$\mathbf{F}^c = \begin{Bmatrix} \sigma_{11}^A b \\ \sigma_{23}^A b \\ \sigma_{22}^A b \\ \sigma_{33}^A b^2 \end{Bmatrix} = \begin{bmatrix} b & 0 & 0 & 0 \\ 0 & b\cos\varphi\sin\varphi & b(\sin^2\varphi - \cos^2\varphi) & -b\cos\varphi\sin\varphi \\ 0 & b\sin^2\varphi & -2b\cos\varphi\sin\varphi & b\cos^2\varphi \\ 0 & b^2\cos^2\varphi & 2b^2\cos\varphi\sin\varphi & b^2\sin^2\varphi \end{bmatrix} \begin{Bmatrix} \sigma_{xx} \\ \sigma_{yy} \\ \sigma_{yz} \\ \sigma_{zz} \end{Bmatrix} \equiv \mathbf{T}\boldsymbol{\sigma}^g \tag{3}$$

where $\mathbf{F}^c$ is the local force vector associated with the common degrees of freedom, the superscript A denotes the average of the surface tractions (t_i) applied to the unit-cell, i.e.

$$\sigma_{11}^A = \frac{\int_{\Gamma_1} t_1 \, dS}{2b}, \quad \sigma_{23}^A = \frac{\int_{\Gamma_2} t_3 \, dS}{2b}, \quad \sigma_{22}^A = \frac{\int_{\Gamma_2} t_2 \, dS}{2b}, \quad \sigma_{33}^A = \frac{\int_{\Gamma_1} t_3 \, dS}{4b^2}, \tag{4}$$

and S denotes surface area. Equations (2) and (4) make up the boundary conditions for the microscale model. Note that the natural and essential boundary conditions are of a mixed form since the u_i^cs of (2) and the traction distributions in (4) serve as the unknown parameters.

Finally, the displacements from the microscale model must be transformed back to the mesoscale coordinate system. The average strains are defined to be

$$\varepsilon^{\Delta}_{11} \equiv \frac{u_1(+b, x_2) - u_1(-b, x_2)}{2b}, \quad \varepsilon^{\Delta}_{23} \equiv \frac{\bar{u}_3(x_1, +b) - \bar{u}_3(x_1, -b)}{4b},$$

$$\varepsilon^{\Delta}_{22} \equiv \frac{u_2(x_1, +b) - u_2(x_1, -b)}{2b}, \quad \varepsilon^{\Delta}_{33} \equiv \varepsilon_{33}. \tag{5}$$

and are transformed back to the y–z coordinate system to obtain,

$$\varepsilon^{g} \equiv \begin{Bmatrix} \varepsilon_{xx} \\ \varepsilon_{yy} \\ \varepsilon_{yz} \\ \varepsilon_{zz} \end{Bmatrix} = \begin{bmatrix} \frac{1}{b} & 0 & 0 & 0 \\ 0 & \frac{2\cos\varphi\sin\varphi}{2b} & \frac{\sin^2\varphi}{b} & \cos^2\varphi \\ 0 & \frac{\sin^2\varphi - \cos^2\varphi}{2b} & \frac{-\cos\varphi\sin\varphi}{b} & \cos\varphi\sin\varphi \\ 0 & \frac{-2\cos\varphi\sin\varphi}{2b} & \frac{\cos^2\varphi}{b} & \sin^2\varphi \end{bmatrix} \begin{Bmatrix} u_1^c \\ u_3^c \\ u_2^c \\ \varepsilon_{33} \end{Bmatrix} \equiv \hat{\mathbf{T}}\mathbf{u}^c. \tag{6}$$

where the boundary surface displacement requirements of (2) were used (considering the first quadrant). One should note that both equilibrium and continuity have been maintained between the microscale and mesoscale using this decomposition. Additionally, this decomposition reduces to the usual result for a homogeneous, isotropic material.

For completeness' sake, mention should be made concerning the separation of the in- and out-of-plane displacements [cf. eqn (1)] for a fiber-reinforced material. An implicit assumption is that the fiber aspect ratio is large with respect to the microscale, since the end effects created by fiber sliding would become important if this were not the case. If there were no tractions developed on the interface (i.e. a perfectly smooth interface), the assumption of (1) would clearly not be reasonable.

3. CONSTITUTIVE MODELS AND PROBLEM STATEMENT

To model the time-dependent rheologic response of the composite, a mechanical constitutive theory is used. The continuum elements of the composite (i.e. the fiber and the matrix) are modeled as a nonlinear Maxwell fluid, which is a model often used to describe the steady-state *shearing* response of metals and ceramics (Cannon and Langdon, 1987),

$$\dot{\varepsilon}_{12} \equiv \dot{\varepsilon}^{e}_{12} + \dot{\varepsilon}^{c}_{12} = \frac{\dot{\sigma}_{12}}{2G} + \lambda\left(\frac{\sigma_{12}}{2G}\right)^{n}, \tag{7}$$

where σ_{12} and ε_{12} indicate stress and strain in pure shear, superscripts e and c denote elastic and creep respectively, the superposed dot denotes the material time rate and λ is an inverse characteristic time, i.e. the ratio of the shear modulus G to some characteristic viscosity. To generalize (7) to three-dimensions for an isotropic material (and small gradients in displacement), an assumption relating to the direction of the creep strains is,

$$\dot{\mathbf{E}}^{c} = \alpha\mathbf{S}, \tag{8}$$

where α is a scalar and $\mathbf{E}$ and $\mathbf{S}$ are the deviatoric strain and stress tensors, respectively. Equation (8) is analogous to the Prandtl–Reuss associated flow rule using a von Mises yield function (Hill, 1950).

By equating the plastic work of a general, three-dimensional deformation with that of pure shear, (7) and (8), along with the following definition of an effective stress:

$$\hat{s} \equiv \sqrt{\frac{\mathbf{S}:\mathbf{S}}{2}} \tag{9}$$

allows the generalized deviatoric constitutive relation to be written as

$$\dot{\mathbf{E}} = \frac{\dot{\mathbf{S}}}{2G} + \lambda\left(\frac{\hat{s}}{2G}\right)^{n}\frac{\mathbf{S}}{\hat{s}}. \tag{10}$$

Employing an assumption of elastic compressibility,

$$\tilde{\sigma} = 3K\tilde{\varepsilon} \tag{11}$$

where the tilde indicates the hydrostatic components and K is the elastic bulk modulus, along with the deviatoric constitutive relation of (10) and the definitions of deviatoric stress and strain, allows the total stress rate tensor to be written as,

$$\dot{\mathbf{T}}(t) = G(\nabla\dot{\mathbf{u}}(t) + \nabla\dot{\mathbf{u}}(t)^{\mathrm{T}}) + (K - \tfrac{2}{3}G)\,\mathrm{tr}\,[\nabla\dot{\mathbf{u}}(t)]\mathbf{I} - 2G\lambda\left(\frac{\hat{s}(t)}{2G}\right)^{n}\frac{\mathbf{S}(t)}{\hat{s}(t)}, \tag{12}$$

where small displacements ($\mathbf{u}$) and small displacement-gradients ($\nabla\mathbf{u}$) are implied.

For an *interface* constitutive law, there are a number of features that must be accounted for if the full deformation behavior of a ceramic composite interface at an elevated temperature is to be considered. These features include (1) debonding in a mixed-mode loading, (2) cavitation (decohesion of the interface) for tensile normal tractions, (3) deformation history dependence, (4) rate-dependent effects for the slip and shearing behavior, and (5) the normal traction dependence of the shearing deformations. Perhaps the simplest constitutive law which considers (2), (3) and (5), is Coulomb friction including interface tensile opening, i.e.

$$|\mathbf{t}_t| \leqslant \mu t_n, \quad \text{for } t_n \leqslant 0, \qquad \mathbf{t} = 0, \quad \text{for } [\![\mathbf{u}]\!]\cdot\mathbf{n} \leqslant 0, \tag{13a, b}$$

where the $[\![\mathbf{u}]\!] \equiv \mathbf{u}^{i} - \mathbf{u}^{j}$ (see Fig. 2), the normal $\mathbf{n} \equiv \mathbf{n}^{i}$ (the outward pointing normal of phase i), tractions are defined as $\mathbf{t} \equiv \mathbf{t}^{i} \equiv \mathbf{T}^{i} \circ \mathbf{n}^{i}$, $\mathbf{t}_n = \mathbf{t}^{i}\cdot\mathbf{n}^{i}$, $|\mathbf{t}_t|$ is the Euclidean norm of the tangential tractions on the surface, and the coefficient of friction μ is assumed to be constant. This constitutive law is implemented using an incremental plasticity formulation, thus a dependence on the deformation history is also maintained. For simplicity, this constitutive law is used in the ensuing analysis to describe the fiber–matrix interface behavior for the

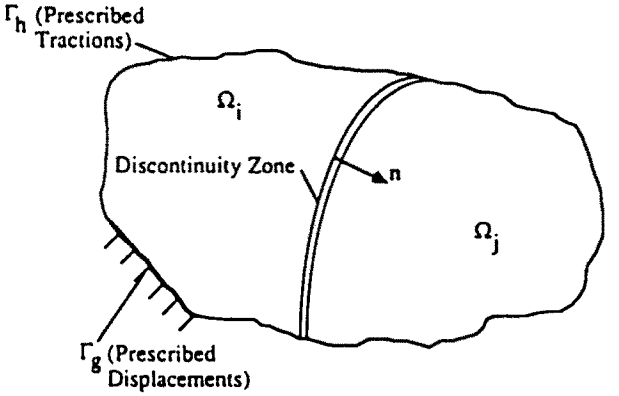

Fig. 2. Variable definitions for the problem description. Here two contacting bodies Ω_i and Ω_j (with prescribed traction and displacement conditions Γ_h and Γ_g, respectively), are separated by an infinitesimally thin discontinuity zone with normal $\mathbf{n}$.

composite, even though it does not consider rate-dependent effects or debonding. The effects of interface debonding are discussed further in Section 5.

With the constitutive laws of (12) and (13), the *general* boundary value problem of n contacting bodies (Ω_i, $i = 1, n$; *c.f.* Fig. 2) can now be stated. The bodies are assumed to be separated by infinitesimally thin interface regions, of which the tractions across these regions are, in general, history dependent (as previously discussed, a rate form is appropriate). For a quasistatic, small-displacement gradient, small-displacement formulation, the problem can be stated as,

For each body $\bar{\Omega}_i$, find a velocity $\dot{\mathbf{u}}_i : \bar{\Omega}_i \to \Re^3$, such that each $\dot{\mathbf{u}}_i \in \delta_i$,

$$\text{where } \delta_i = \left\{ \dot{\mathbf{u}} | \nabla \circ \mathbf{T} + \dot{\mathbf{f}} = 0 \text{ on } \Omega_i, \right.$$

$$\dot{\mathbf{u}} = \dot{\mathbf{g}} \text{ on } \Gamma_g \cap \bar{\Omega}_i, \ \dot{\mathbf{T}} \circ \mathbf{n}^i = \dot{\mathbf{h}} \text{ on } \Gamma_h \cap \bar{\Omega}_i,$$

$$\left. [\![\dot{\mathbf{t}}]\!] = 0 \text{ and } [\![\dot{\mathbf{u}}]\!] \cdot \mathbf{n} \leqslant 0 \text{ on } \sum_{j=1, i \neq j}^{n} \bar{\Omega}_i \cap \bar{\Omega}_j \text{ if } \int_0^t [\![\dot{\mathbf{u}}(\tau)]\!] \cdot \mathbf{n} \, d\tau = 0 \right\}, \tag{14}$$

where the stress derivative is defined in (12), the $\dot{\mathbf{u}}_i$ are assumed to be sufficiently smooth such that the required derivatives exist, the bar indicates the closure of the region, $\Re^3$ indicates three-dimensional real space, $\mathbf{f}$ indicates the body force, Γ_g is the surface over which velocities are prescribed (see Fig. 2), Γ_h is the surface over which traction rates are prescribed, and outward pointing normals have been defined as positive. Using (13) the interface tractions are formulated in terms of displacement jumps in the following section.

4. CONTACT FRICTION TREATMENT

The contact friction is treated using a nonassociated-flow-rule plasticity formulation with a penalty method for enforcing the infinitesimally thin character of the interface. This development is for the non-opening interface, i.e. (13a) [(13b) will be treated as a prescribed zero-traction condition at the end of this section]; the treatment is an extension of the work by Plesha *et al.* (1989). Appendix A summarizes the development of the incremental theory. Note that this treatment differs from that of Achenbach and Zhu (1989); they examined the role of a finite interphase between the fiber and matrix by varying $\mathbf{E}^c$ in the case of a tensile loading perpendicular to the fiber direction. We are using an infinitesimally thin interphase.

One of the implicit assumptions for the incremental solution methodology derived in Appendix A is that of a well-defined yield surface and corresponding slip direction; specifically, the derivative of the slip potential given in (A.3) must exist (i.e. the yield surface cannot be singular). The composites problem does not satisfy this requirement for the solution during the initial loading for the idealized Coulomb friction law of Fig. 3(a). To illustrate this point, consider the unit-cell representation of Fig. 1 for a two-dimensional loading case ($\varphi = 90°$) with full bonding between the fiber and matrix and let the fiber and matrix have identical elastic properties. With the appropriate transformations, it can be

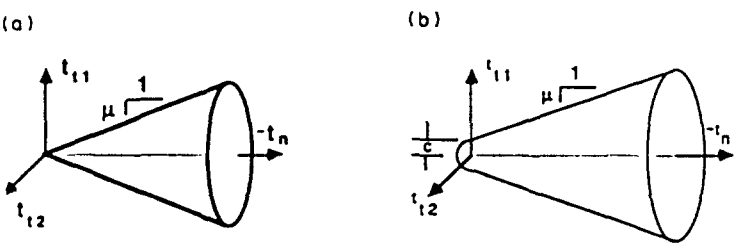

Fig. 3. Interface constitutive laws: (a) Perfect Coulomb friction. (b) Coulomb friction plus a cohesive strength, c.

shown that the normal and shear tractions along the interface are given by $t_n = -\sigma_{yy}\cos^2\vartheta$ and $t_t = \sigma_{yy}\cos\vartheta\sin\vartheta$, respectively (the angle ϑ is defined in the inset of Fig. 6). Thus for the idealized Coulomb friction, as illustrated in Fig. 3(a), the ratio $-t_t/t_n = \tan\vartheta$ provides the minimum value of the friction coefficient that will prevent slip from occurring. Since $\tan\vartheta$ approaches infinity as ϑ approaches 90°, slip will occur for an infinitely small amount of loading.

It is clear that an analysis of the composites debonding problem would be formidable, thus an idealization must be made in the constitutive relation as it pertains to debonding. The approach pursued here is to simply ignore the debonding question completely for the initial step loading of the composite, and use an idealized Coulomb friction model as presented in (13) (Fig. 3(a)). To avoid the singularity of the yield surface, one could artificially redefine the yield surface with some unknown cohesive strength, as shown in Fig. 3(b). A computationally superior option would be to make the assumption of proportional stressing, similar to that proposed by Hencky for associated plasticity [e.g. Chakrabarty (1987)],

$$\mathbf{T}(t) = \alpha(t)\mathbf{T}, \tag{15}$$

where $\alpha(t)$ is a scalar loading parameter. This approach is pursued here.

To develop a solution methodology, based upon the assumption of proportional stressing, that is compatible with the incremental formulation of Appendix A, the governing equations given in the incremental formulation are integrated as follows:

$$[\![\dot{\mathbf{u}}]\!] = [\![\dot{\mathbf{u}}]\!]^e + [\![\dot{\mathbf{u}}]\!]^s \rightarrow [\![\mathbf{u}]\!] = [\![\mathbf{u}]\!]^e + [\![\mathbf{u}]\!]^s, \qquad \dot{\mathbf{t}} = \mathbf{E}^e[\![\dot{\mathbf{u}}]\!]^e \rightarrow \mathbf{t} = \mathbf{E}^e[\![\mathbf{u}]\!]^e, \tag{16a, b}$$

$$[\![\dot{\mathbf{u}}]\!]^s = \Lambda\frac{\partial H}{\partial t} \rightarrow [\![\mathbf{u}]\!]^s = \hat{\Lambda}\frac{\partial H}{\partial t}, \qquad F = 0 \quad \text{and} \quad \dot{F} = 0 \rightarrow F = 0. \tag{16c, d}$$

Combining (16a) (16c) to obtain,

$$\mathbf{t} = \mathbf{E}^e\left([\![\mathbf{u}]\!] - \hat{\Lambda}\frac{\partial H}{\partial t}\right), \tag{17}$$

and requiring $\mathbf{t}$ to satisfy the yield criterion [i.e. (16d) for which F is given in (A4)], gives,

$$t_n = E_n[\![u_n]\!], \quad t_{tt} = \frac{E_t[\![u_{tt}]\!]}{\left(1 + \dfrac{\hat{\Lambda}E_t}{-\mu E_n[\![u_n]\!]}\right)}. \tag{18}$$

Using the yield condition with (18), $\hat{\Lambda}$ is written in terms of relative displacement jumps, and substituted back into (17) thus allowing the tractions to be written as a function of the relative displacements,

$$\mathbf{t} = \dot{\mathbf{E}}[\![\mathbf{u}]\!],$$

where

$$\dot{\mathbf{E}} = \begin{bmatrix} E_n & 0 & 0 \\ 0 & \dfrac{-\mu E_n[\![u_n]\!]}{\|[\![\mathbf{u}_t]\!]\|} & 0 \\ 0 & 0 & \dfrac{-\mu E_n[\![u_n]\!]}{\|[\![\mathbf{u}_t]\!]\|} \end{bmatrix}, \tag{19}$$

with $\|[\![\mathbf{u}_t]\!]\|$ indicating the Euclidean norm of the tangential displacement jumps. When combined with the yield and separation conditions given in (13), the full constitutive law for the deformation theory is written as,

$$\mathbf{t} = \mathbf{E}^{cp}[\![\mathbf{u}]\!],$$

where

$$\mathbf{E}^{cp} = \begin{cases} \mathbf{E}^{e}, & [\![\mathbf{u}]\!]\cdot\mathbf{n} > 0;\ F < 0, \\ \hat{\mathbf{E}}, & [\![\mathbf{u}]\!]\cdot\mathbf{n} > 0;\ F = 0, \\ \mathbf{0}, & [\![\mathbf{u}]\!]\cdot\mathbf{n} \leqslant 0. \end{cases} \tag{20}$$

By neglecting the viscoelasticity term (i.e. a step loading function in time), (14) can also be integrated in time, which, when coupled with (20), gives a nonlinear, displacement-based equation; a numerical algorithm used for solving this equation is developed in Meyer *et al.* (1992b).

5. SOLUTION METHODOLOGY

The solution of the unit-cell boundary value problem described above is approximated by using a finite element discretization over the continuum and interface surfaces (Qiu *et al.*, 1991). The final form of the discretized equations is outlined in Appendix B. This discretization is coupled with a Newton–Raphson algorithm for the initial solution [eqns (20) and an integrated form of (14)], and a radial corrector algorithm for the incremental solution [eqns (A6) and (14)].

The nonassociated flow rule of (A5) results in a boundary value problem which is not self-adjoint, therefore the resulting stiffness matrix is nonsymmetric. Figure 4 illustrates the profile of the stiffness matrix due to the effects of the boundary conditions given in (2). A specialized equation solver which takes advantage of the sparsity of the stiffness matrix was devised (Meyer *et al.*, 1992b).

6. LOAD RELAXATION

By partitioning the stiffness matrix as illustrated in Fig. 4 and using the transformations of (3) and (6), the discretized equations are rewritten in terms of the mesoscale strains and stresses,

$$\begin{bmatrix} \mathbf{K}_{AA} & \mathbf{K}_{AB} \\ \mathbf{K}_{BA} & \mathbf{K}_{BB} \end{bmatrix} \begin{Bmatrix} \dot{\mathbf{d}}^{A} \\ \dot{\mathbf{u}}^{c} \end{Bmatrix} = \begin{Bmatrix} \dot{\mathbf{F}}^{A} \\ \dot{\mathbf{F}}^{c} \end{Bmatrix} \Rightarrow \begin{bmatrix} \mathbf{K}_{AA} & \mathbf{K}_{AB}\hat{\mathbf{T}}^{-1} \\ \mathbf{T}^{-1}\mathbf{K}_{BA} & \mathbf{T}^{-1}\mathbf{K}_{BB}\hat{\mathbf{T}}^{-1} \end{bmatrix} \begin{Bmatrix} \dot{\mathbf{d}}^{A} \\ \dot{\boldsymbol{\varepsilon}}^{g} \end{Bmatrix} = \begin{Bmatrix} \dot{\mathbf{F}}^{A} \\ \dot{\boldsymbol{\sigma}}^{g} \end{Bmatrix} \tag{21}$$

where $\mathbf{d}^{A}$ and $\mathbf{F}^{A}$ are the displacement and force vectors associated with the internal degrees of freedom [c.f. eqns (1) and (2)]. One should note the lack of symmetry in the transformed stiffness (i.e. the transformation matrices are unsymmetric). With this formulation, the strain rate $\dot{\varepsilon}_{yy}$ can be prescribed in the simulation of load relaxation.

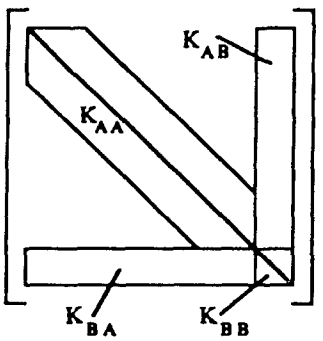

Fig. 4. Stiffness matrix profile. The unsymmetric block $\mathbf{K}_{AA}$ corresponds to the general common degrees of freedom; the other three blocks relate to the common degrees of freedom, i.e. ε_{33}, and the u_i^c of eqn (2).

7. RESULTS AND DISCUSSION

The modeling results presented in this section were obtained by discretizing the unit-cell problem of Fig. 1(b) with quadratic elements as illustrated in Fig. 5. The solutions using the iterative and time integration techniques described in Meyer *et al.* (1992b) were obtained using the Astronautics Corporation of America Super-Mini Computer® at the University of Wisconsin–Madison.

The modeling results will be presented as follows. First, a case study is presented for a Newtonian response (i.e. the stress exponent $n = 1$), both for creep and load relaxation. The effects of the fiber orientation angle and the friction coefficient are demonstrated using material properties that resemble those of the SiC (Nicalon)–alkaline earth aluminosilicate glass–ceramic composite system. The Nicalon fiber is modeled as elastic [i.e. $\lambda = 0$], with the properties of, $E_f = 97$ GPa, $\nu_f = 0.2$, and the calcium aluminosilicate glass–ceramic matrix is modeled as a nonlinear Maxwell fluid (linear for $n = 1$), with the initial elastic properties of $E_m = 37$ GPa, $\nu_m = 0.34$. The selection of these properties is discussed further in Meyer *et al.* (1992a). Following the study of the Newtonian response is an examination of the effect of the stress exponent for flow of the matrix, when varied from 1 to 3. Finally, a sensitivity study is presented that explores the effects of changing the initial material parameters.

To illustrate the stress field variations during the creep response of the composite model *without* slip or separation, Fig. 6 contains the time history for the interface tractions versus circumferential location, for a fiber orientation angle of $\varphi = 60°$. One should note that in the normal pressure evolution the compressive tractions near the top of the fiber increase in magnitude, as do the tensile tractions on the side, with a point near $\vartheta = 42°$ remaining unchanged. The evolution also indicates that a steady-state stress field is achieved. Small pressure oscillations were observed (most notably the in-plane (x_1, x_2) shear, Fig. 6(b)) due to the elastic compressibility assumption of (11), which, in the case of the steady-state flow, acts as an incompressible flow constraint, giving rise to spurious pressure modes. A reduced integration technique (constant pressures) on the quadratic triangles was used (Cook *et al.*, 1989) with an inter-element averaging scheme for pressure smoothing along the interface.

Figure 7 illustrates the same configuration as Fig. 6 for the case of a fully-debonded fiber with a friction coefficient of $\mu = 0.1$. In this case a region of opening exists (i.e. cavitation), with the contacting region extending from $\vartheta = 0°$ to approximately $\vartheta = 50°$, and receding during the time-dependent deformation to a steady-state value of $\vartheta = 37°$ (cavitation will be explored later). Also, as in the bonded case, regions of increase are noted in the normal tractions. One should also be aware that the interface is in a condition of full

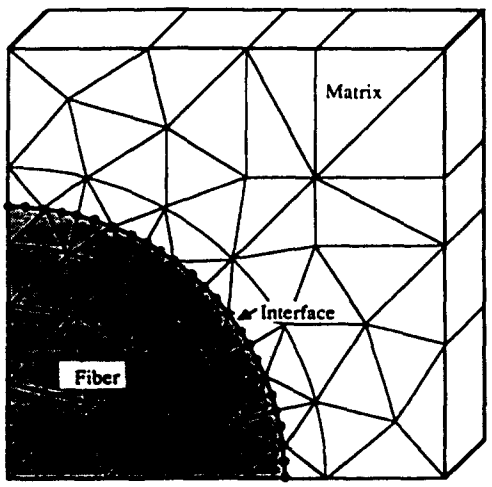

Fig. 5. A finite element spatial discretization of Fig. 1(b). The continuum and contact surface were discretized using 82 quadratic triangles and 12 quadratic contact elements, corresponding to 630 degrees of freedom. The dimensions selected correspond to a volume fiber fraction of 30%.

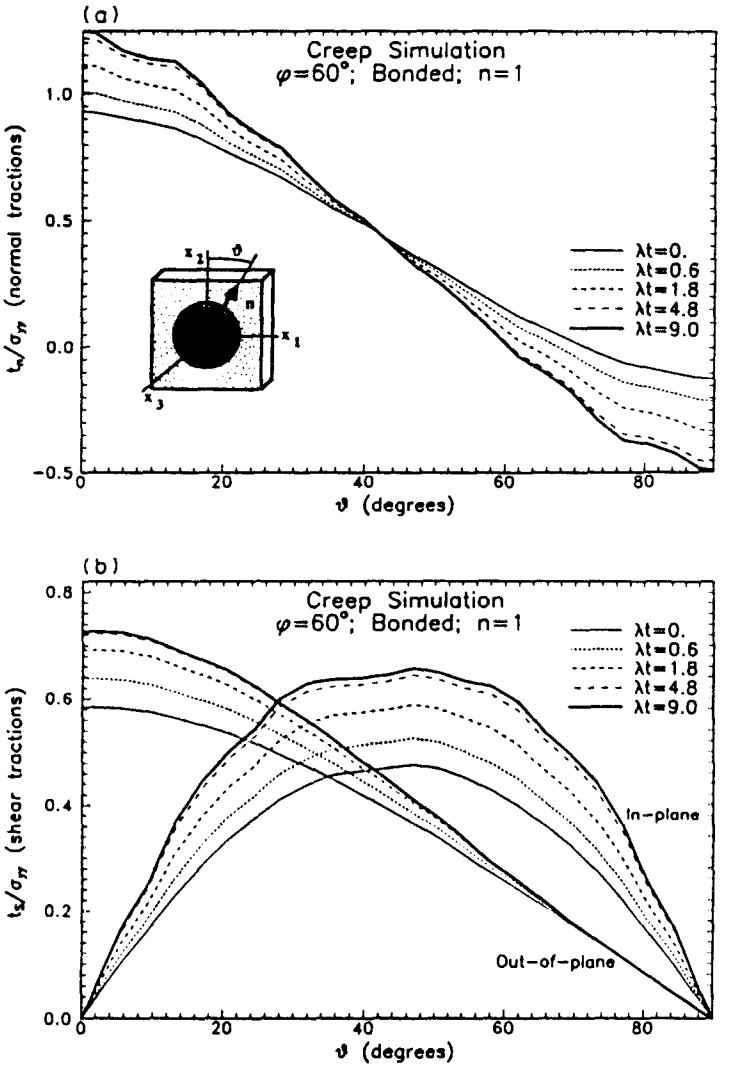

Fig. 6. The evolution of the interface tractions during creep; a bonded interface condition ($n = 1$, $\varphi = 60°$, see text for material properties): (a) Normal tractions. (b) Shear tractions (in-plane x_1, x_2; out-of-plane n, x_3). Observe the increase in tensile normal tractions near $\vartheta = 90°$, and the increase in the magnitude of the compressive normal tractions near $\vartheta = 0°$. Also apparent is the existence of a steady-state stress field.

slip in the initial solution, and the condition of $\dot{F} = 0$ is satisfied during the entire simulation. From Fig. 7, note the in-plane tractions, which were the same order of magnitude as the out-of-plane tractions (t_3) for the bonded case, drop to only 20% of the out-of-plane tractions for the debonded case; this indicates the ratio of the out-of-plane to the in-plane compliance is very high, which is somewhat intuitive. Also, one should observe that the tractions increase approximately 40% from the initial to the steady-state solution in the debonded case, compared to only 20% for the bonded case. As a final remark, note the time evolution of the in-plane tractions, with the final curves exhibiting maximums near the ends, rather than a single maximum near the center.

The far-field displacements are summarized in Fig. 8 for the conditions of Figs 6 and 7, with the three, steady-state strain rate values noted in the legend. First, one should note that although the stress fields change substantially during creep, the far-field displacement values show only small changes during the time evolution; predicted deformation transients are very small. This behavior is somewhat intuitive if the compatibility constraints stipulated in eqn (2) are recalled, and also from Figs 6 and 7 in that the integral of the tractions around the interface do not change substantially with time. Both of these factors act to reduce the sensitivity of the far-field displacements to the time redistribution of the tractions.

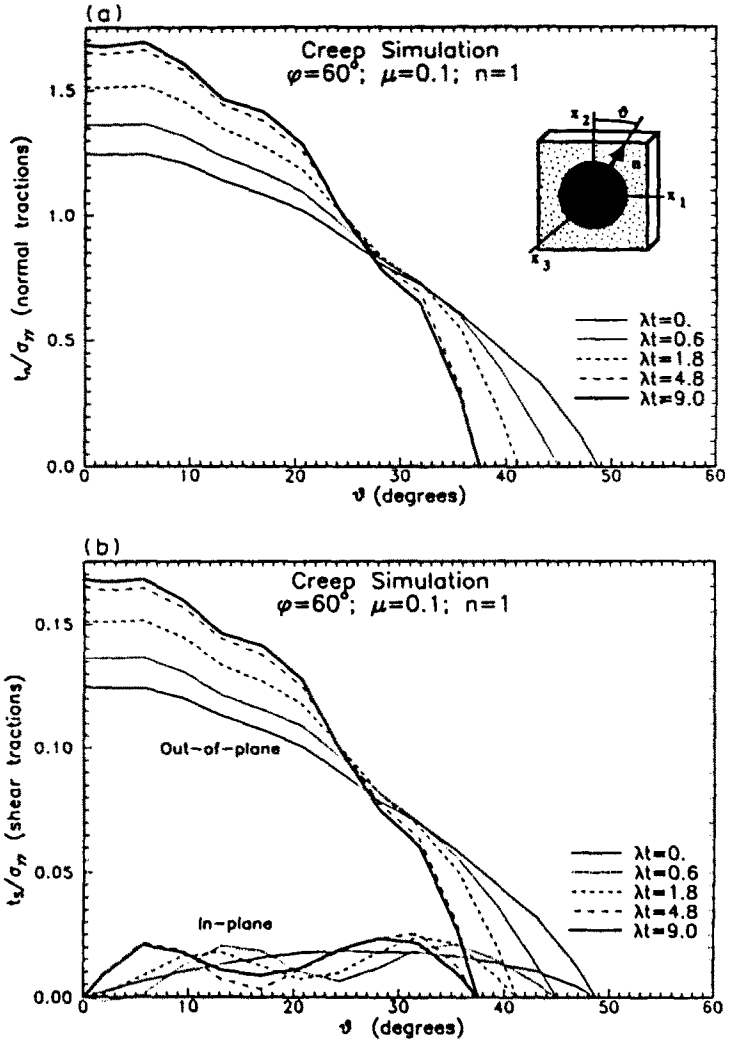

Fig. 7. The evolution of the interface tractions during creep; a fully debonded interface condition [$\mu = 0.1$, $n = 1$, $\varphi = 60^\circ$]: (a) Normal tractions. (b) Shear tractions. A region of increase and a region of decrease are present, with a cavitation region growing from $\vartheta = 50^\circ$ to $\vartheta = 37^\circ$ at the steady-state.

Figure 9 has been included to illustrate a case where the far field displacement transients are more pronounced, namely for a bonded interface and a fiber orientation angle of $\varphi = 90^\circ$. A much stronger time-history effect is present than in Fig. 8, both in the longitudinal direction and in the direction of the fibers. The transverse strain rate ($\dot{\varepsilon}_{zz}$) approaches zero, as expected, since the elastic fiber constrains the matrix material from additional deformation in the fiber direction.

If the interface deformation is to be ascertained with the modeling just prescribed, the relationship of the far-field displacements and the fiber orientation angle (φ) must be explored. The far-field displacement-related quantity that seems most amenable for this study (both analytically and experimentally) is the steady-state strain rate. To illustrate, Figs 10(a-c) demonstrate the relationship between three steady-state strain rates (normalized by λ) plotted as a function of the fiber orientation angle, for varying interface conditions. One immediate observation is that the creep rates become more sensitive to the fiber orientation angle as the friction coefficient (μ) decreases. Also, the strain rate is most sensitive to the interface conditions between $\mu = 0.2$ and $\mu = 1.0$ for a constant fiber orientation angle. This result illustrates that, although the far-field displacements are not sensitive to the traction redistribution as previously discussed, they are sensitive to the magnitude of the shear tractions developed, which, in turn, are dependent upon the friction coefficient. The

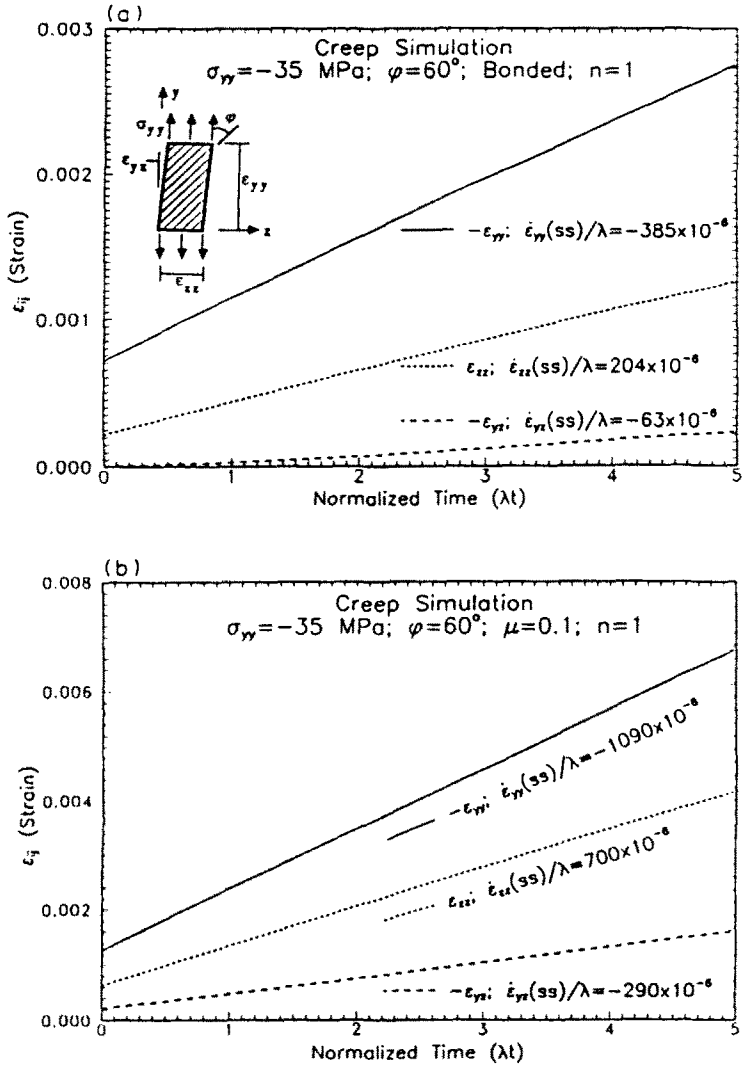

Fig. 8. Creep simulation [$n = 1$, $\varphi = 60$]: (a) Bonded interface condition. (b) Fully debonded with $\mu = 0.1$. The three independent displacement variables show only small transients for both cases.

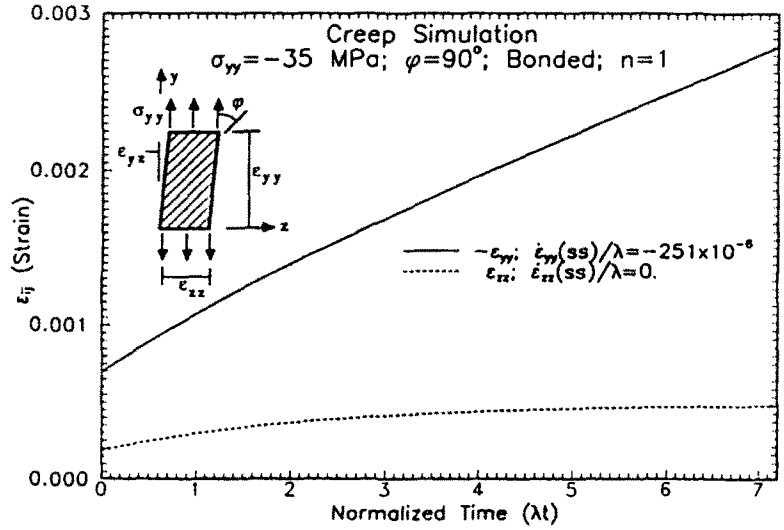

Fig. 9. Creep simulation [$n = 1$, $\varphi = 90$]: a bonded interface condition. A significant transient is observable, note the transverse strain rate approaches zero, since the fiber behavior is elastic.

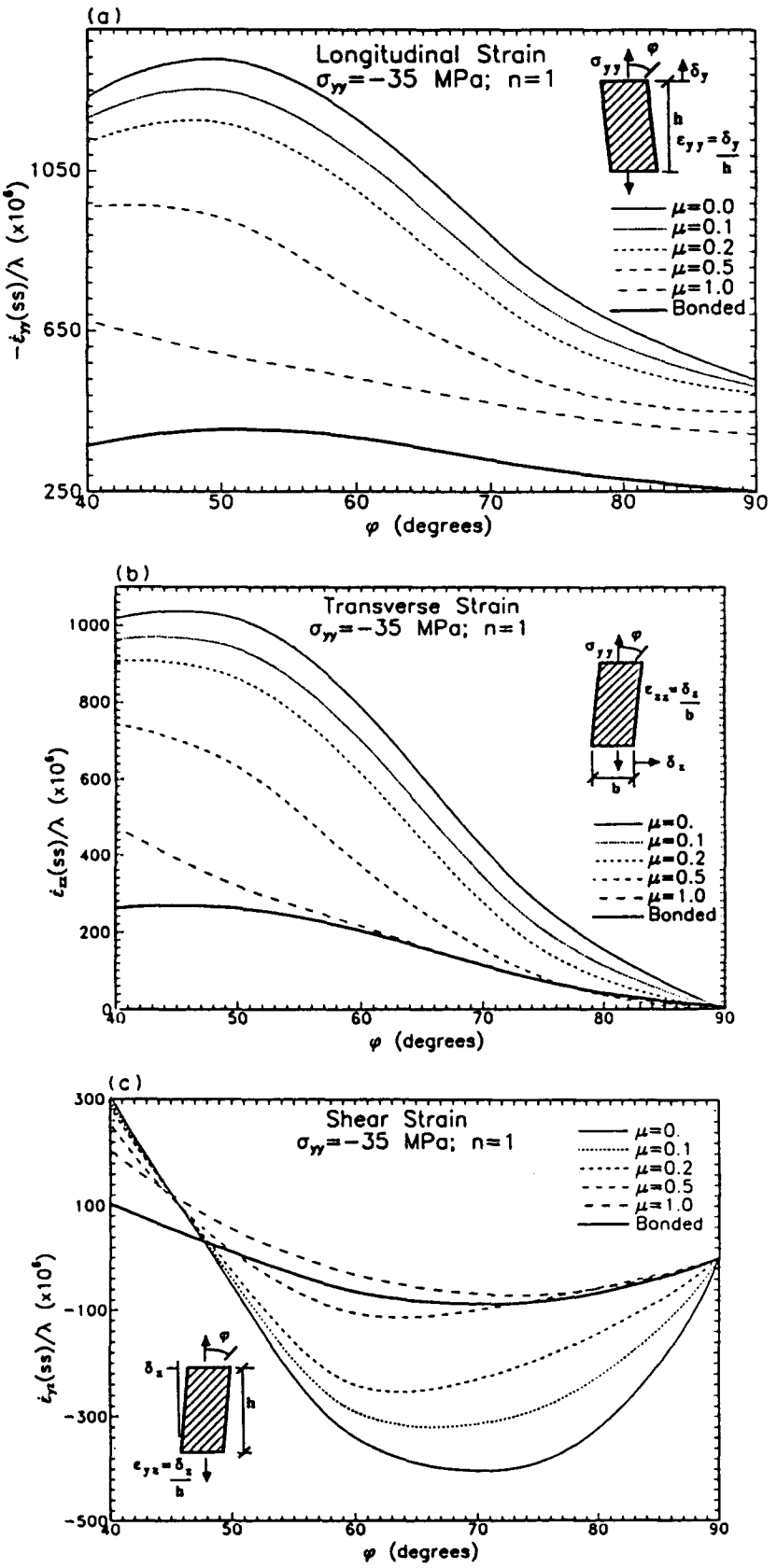

Fig. 10. The dependence of the steady-state strain rate on the fiber angle (n = 1): (a) Longitudinal strain. (b) Transverse strain. (c) Shearing strain. (d) Normalized longitudinal strain. The curves were constructed using a tight-spline fit through 5 points at φ = 90°, 75°, 60°, 50° and 40°. The strain rate sensitivity to the fiber orientation angle is seen to increase with a decreasing coefficient of friction for all cases.

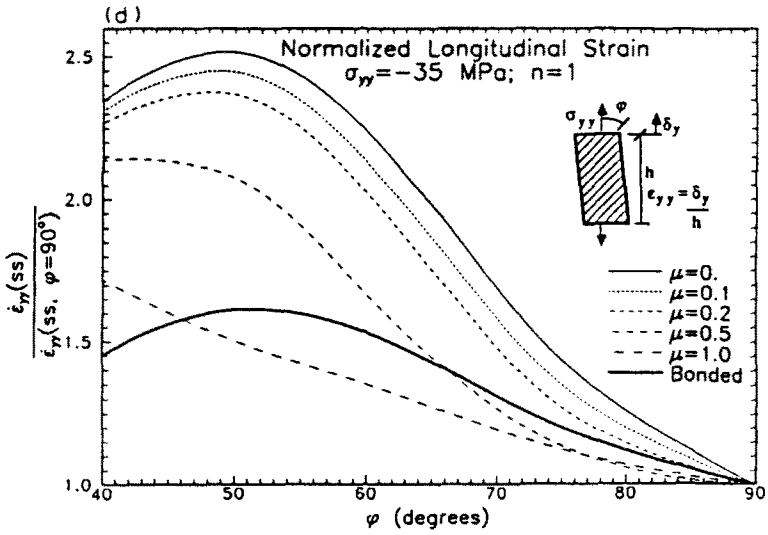

Fig. 10.—*Continued.*

transverse and shear strains illustrated in Figs 10(b,c) are significant in that the final specimen shape can be predicted and correlated with the experimentally observed shape. One should note that the magnitude of the predicted shear distortions are much smaller than the longitudinal distortions. It should be further noted that the fully bonded case is not the extremum as one may at first expect. The difference between full fiber bonding and debonding with a large friction coefficient is the region of tensile bonding, apparent in Fig. 6 (discussed shortly).

Finally, to aid in correlating with experimental results, Fig. 10(d) illustrates the longitudinal strain rates normalized to the strain rates of the $\varphi = 90°$ simulation. (This normalization eliminates the shear viscosity of the matrix, i.e. λ.) One interesting observation is the change in the basic shape of the curves; for the bonded and low friction interface conditions the extremum of the curves do not occur at the endpoints, in contrast to the behavior for the high friction interface conditions. The normalized strain rates will be discussed further in the non-Newtonian response presentation.

Another interesting feature of the creep simulations is the growth of cavitation regions surrounding the sides of the fiber. Figure 11 is a time evolution of the cavitation regions forming during creep for $n = 1$ and fiber orientation angles of $\varphi = 40°$ and 90°. The regions continue to increase during the creep, with the cavitation region of the $\varphi = 90°$ case being larger than the $\varphi = 40°$ case. By comparing Figs 10(a) and 11, it can be concluded that the size of the cavitation at $\vartheta = 90°$ is

$$[\![u_n]\!] \sim -\varepsilon_{yy} b; \quad \text{(where } b \equiv \text{unit cell dimension)}. \tag{22}$$

This relation has been used to quantify the amount of cavitation observed experimentally in Meyer *et al.* (1992a).

For load relaxation, the history dependence of the interface constitutive model requires that the prior history be stated, e.g. a step loading, a steady-state creep established before the relaxation, or some combination thereof. Figure 12(a) illustrates the real time behavior for fiber orientation angles of $\varphi = 60°$ and 90°, with varying interface conditions, after steady-state creep is achieved [$n = 1$]. Comparing with the pure matrix relaxation, a significant effect of the interface condition and fiber orientation angle is observed. Figure 12(b) illustrates the *apparent* stress exponent again for $\varphi = 60°$ and 90°. For the $\varphi = 90°$ fully bonded case the apparent stress exponent is approximately 70% higher than for the matrix only. The apparent stress exponent is only negligibly different from the matrix value for the low fiber orientation angles since the response is more sensitive to the matrix creeping

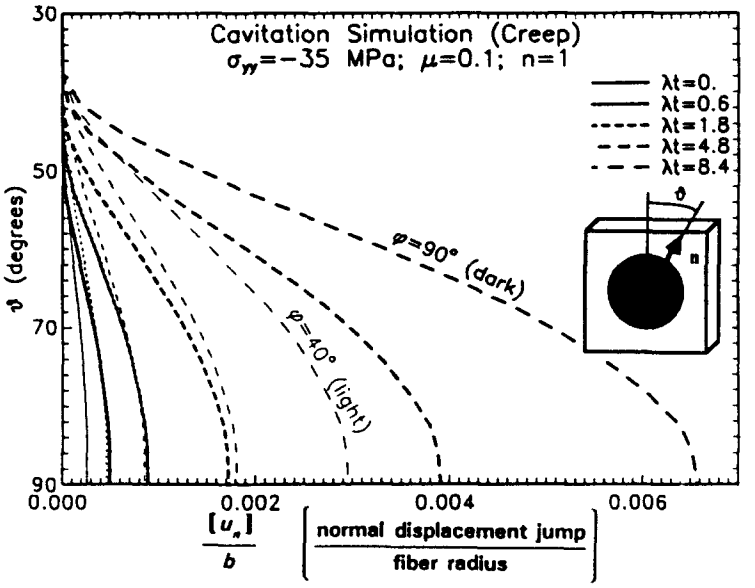

Fig. 11. An illustration of interface cavitation for two fiber orientation angles [n = 1, μ = 0.1], normalized with respect to the fiber radius. The amount of cavitation is smaller for the φ = 40° case, due to the in-plane stresses being lower and due to the slip direction of the contacting region being primarily out-of-plane (c.f. Fig. 6 and eqn (A4)).

behavior. Finally, it is also observed that the apparent stress exponent approaches 1 as the local stress rate decreases.

The sensitivity of the steady-state strain rate to the fiber orientation angle for a non-Newtonian matrix rheology is illustrated in Fig. 13 for three interface conditions and using the normalized strain rate approach of Fig. 10(d). The sensitivity is quite dramatic for low fiber orientation angles and small amounts of interfacial friction, however for the high friction coefficients and the fully bonded interface condition the stress exponent has only a small effect. The load relaxation results are similar to those outlined for n = 1; as an example the apparent stress exponent varies in the four cases illustrated above from 2.9 to 3.8 using a matrix stress exponent of 3. The traction evolution is similar to those illustrated for n = 1.

The model results presented using the steady-state creep rates are dependent upon six independent quantities: the four initial material constants for the fiber and the matrix, the stress exponent (n), and the friction coefficient (μ). It should be noted that a determination of the initial material constants within the composite is difficult experimentally, and in addition, a large degree of anisotropy is thought to exist within the fibers. Thus, any sensitivity of the model to the selected material constants would be a very serious limitation for assessing the interface and creep behavior. For this reason, a sensitivity study was undertaken to examine the effects of changing each of the material parameters. For all four material parameters, a variation of 25% produces less than a 1% change in the steady-state creep rates of Fig. 10: however, as one would expect, a substantial change is observed in the total strains. In addition, the change in the material parameters has a substantial effect on the real time load relaxation behavior of Fig. 12(a), however, the apparent stress exponents of Fig. 12(b) are only slightly affected. These observations along with the debonding discussion in Section 4 lead to the conclusion that the steady-state creep rate and the apparent stress exponent are the appropriate quantities for this analysis!

With the modeling sensitivities just presented, the determination of the interface response using the method prescribed can be summarized by noting that the steady-state strain rate dependence on the fiber orientation angle is a function of two intrinsic material parameters, the coefficient of friction μ and the stress exponent n. By analysing the composite behavior in creep and load relaxation tests, these two parameters can be determined. Thus, the analysis just presented allows for not only *quantifying* the interface behavior, but also

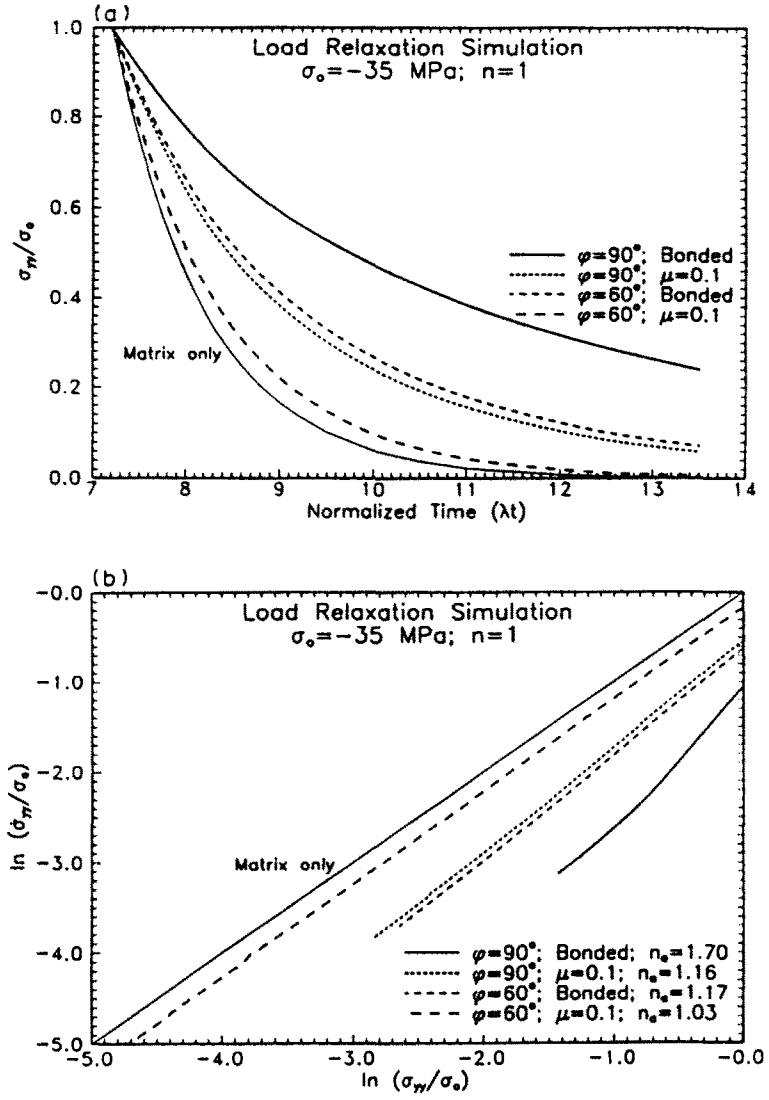

Fig. 12. A simulation of load relaxation following steady-state creep ($\sigma_0 \equiv$ initial compressive stress in y direction]: (a) Real time. (b) Illustration of *apparent* stress exponent, n_a. Figure (b) illustrates that the fibers with a bonded interface can have a significant impact on the measured stress exponent for high fiber orientation angles.

it is useful for *quantifying* the *in situ* creeping behavior of the matrix material within the composite!

8. EXPERIMENTAL CORRELATION

Figure 14 contains the experimental results for Meyer *et al.* (1992a), plotted with the normalized analytical curves for four varying interface conditions and a stress exponent of $n = 3$. The puissance of this method is apparent not only for assessing the interfacial response but also for assessing the creeping behavior of the context of the nonlinear Maxwell fluid. Clearly the interface is debonded (substantiated by microscopy work), and furthermore it is apparent that the other extreme of frictionless sliding does not occur. The slight discrepancy of the model for the fiber orientation angle of $\varphi = 60°$ may be attributed to the inability to fully facilitate translation of the specimen ends; this idea is discussed further in Meyer *et al.* (1992a).

Using a stress exponent of $n = 3$ (obtained from the experimental relaxation data), the model predicts a friction coefficient of $\mu = 0.7$ at 1300°C and decreasing to 0.4 at 1310°C. Previous nanoindenter experiments on similar composite systems have resulted in values from $\mu = 0.1$ to 1.0 (Bright *et al.*, 1989; Marshall and Oliver, 1987).

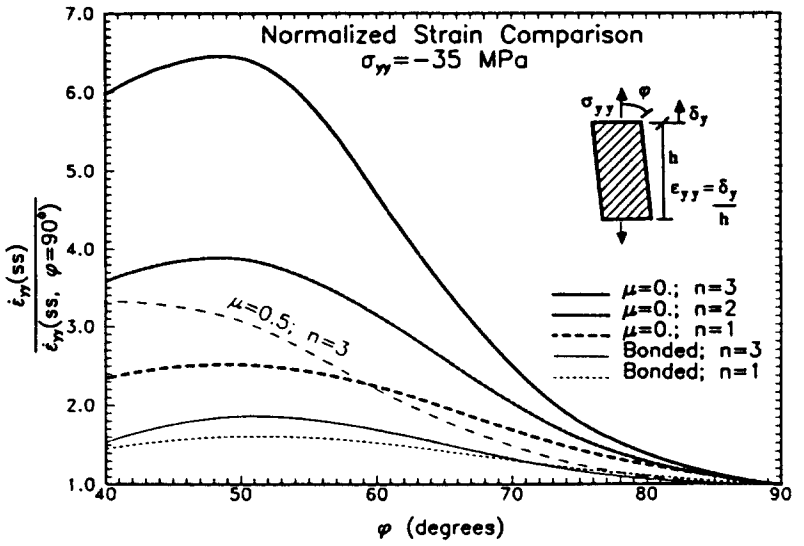

Fig. 13. The sensitivity of the normalized strain rates to various stress exponents. A dramatic difference is observed for small amounts of interface friction, while virtually no difference is observed for the other extreme of a bonded interface. The $\mu = 0.5$ case for $n = 3$ has been included to illustrate the friction sensitivity in the non-Newtonian case.

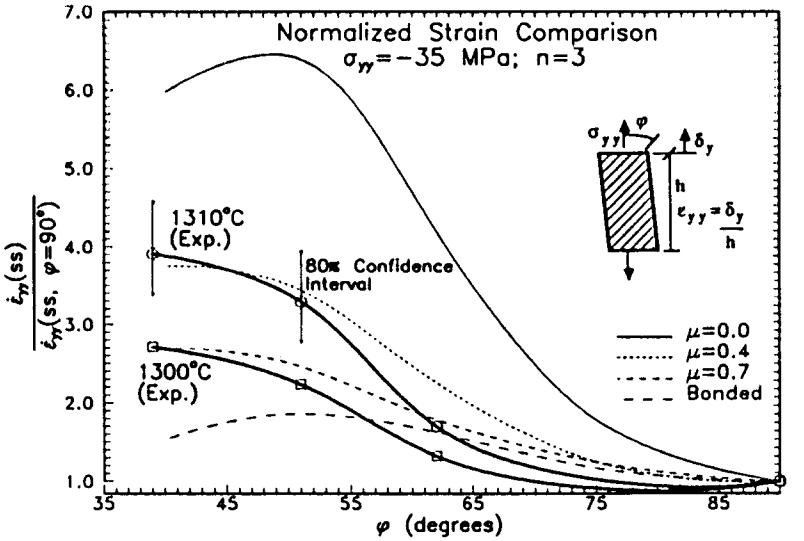

Fig. 14. An experimental comparison from Meyer *et al.* (1992a) ($n = 3$). The predictive ability of the interface condition should be noted. The comparison indicates the interface friction coefficient to be approximately $\mu = 0.4$ to 0.7, with a substantial temperature variation.

Several modifications that may lead to an improved model with a more accurate prediction of the creep and relaxation behavior include: (1) an improved constitutive model for the matrix (including a model for residual glass effects), (2) possible anisotropic response of the composite due to fabrication (i.e. unidirectional pressing), and (3) a larger fiber grouping model, such as a triangle packing model (Brockenbrough *et al.*, 1991). Lower fiber angles could also be examined, however precautions should be taken to ensure a homogeneous deformation of the fiber-matrix system [i.e. microfiber buckling could become an important deformation mechanism in the composite as $\varphi \to 0^\circ$ (Steif, 1988)].

9. CONCLUSIONS

The solution of the creep/load relaxation behavior of a ceramic composite given a non-Newtonian rehology and a non-linear interface slip mechanism at the fiber–matrix interface

has been solved through the use of a penalty method coupled with a deformation and incremental plasticity theory. The results indicate that the interface mechanical behavior can be evaluated in creep/load-relaxation tests on bulk composite specimens. With a proper characterization of the constitutive parameters, the full interface behavior can be evaluated at elevated temperatures.

Acknowledgements—This work was carried out in the course of research sponsored by the U.S. Army Research Office through its URI grant to the Engines Research Center at the University of Wisconsin-Madison.

REFERENCES

Aboudi, J. (1989). Micromechanical analysis of composites by the method of cells. *Appl. Mech. Rev.* **42**, 193–221.

Achenbach, J. D. and Zhu, H. (1989). Effect of interfacial zone on mechanical behavior and failure of fiber-reinforced composites. *J. Mech. Phys. Solids* **37**, 381–393.

Aveston, J., Cooper, G. A. and Kelly, A. (1971). Single and multiple fracture. In *The Properties of Fibre Composites*, pp. 15–26. IPC Science and Technology Press, Surrey, England.

Bright, J. D., Shetty, D. K., Griffin, C. W. and Limaye, S. Y. (1989). Interfacial bonding and friction in silicon carbide [filament]-reinforced cermic- and glass–matrix composites. *J. Am. Ceram. Soc.* **72**, 1891–1898.

Brockenbrough, J. R., Suresh, S. and Wienecke, H. A. (1991). Deformation of metal-matrix composites with continuous fibers: geometrical effects of fiber distribution and shape. *Acta Metall. Mater.* **39**, 735–752.

Budiansky, B., Hutchinson, J. W. and Evans, A. G. (1986). Matrix fracture in fiber-reinforced ceramics. *J. Mech. Phys. Solids* **34**, 167–189.

Cannon, R. W. and Langdon, T. G. (1987). Review: creep of ceramics. *J. Mater. Sci.* **23**, 1–20.

Chakrabarty, J. (1987). *Theory of Plasticity*. McGraw-Hill, New York.

Christensen, R. M. (1979). *Mechanics of Composite Materials*. Wiley, New York.

Chyung, K., Cooper, R. F., Gadkaree, K. P., Stewart, R. L. and Taylor, M. P. (1986). United States Patent, No. 4,615,987.

Cook, R. D., Malkus, D. S. and Plesha, M. E. (1989). *Concepts and Applications of Finite Element Analysis* (3rd Edn). Wiley, New York.

Curnier, A. (1984). A theory of friction. *Int. J. Solids Structures* **20**, 637–647.

Dragone, T. L. and Nix, W. D. (1990). Geometrix factors affecting the internal stress distribution and high temperature creep rate of discontinuous fiber reinforced metals. *Acta Metall. Mater.* **38**, 1941–1953.

Evans, A. G., He, M. Y. and Hutchinson, J. W. (1989). Interface debonding and fiber cracking in brittle matrix composites. *J. Am. Ceram. Soc.* **72**, 2300–2303.

Evans, J. T., Ningyun, W. and Chandler, H. W. (1990). Creep of fiber composite beams in bending. *Acta Metall. Mater.* **38**, 1565–1572.

Goto, S. and McLean, M. (1991). Role of interfaces in creep of fibre-reinforced metal matrix composites-I. Continuous fibres. *Acta Metall. Mater.* **39**, 153–164.

Hill, R. (1950). *Mathematical Theory of Plasticity*. Clarendon Press, Oxford.

Marshall, D. B. and Oliver, W. C. (1987). Measurement of interfacial mechanical properties in fiber-reinforced ceramic composites. *J. Am. Ceram. Soc.* **70**, 542–548.

Meyer, D. W., Cooper, R. F. and Plesha, M. E. (1992a). An off-axis compression test evaluation of the time-dependent and interfacial response of a ceramic composite. *Acta Metall. Mater.* (submitted).

Meyer, D. W., Plesha, M. E. and Cooper, R. F. (1992b). A contact friction algorithm including nonlinear viscoelasticity and a singular yield surface provision. *Comput. Struct.* **42**(6), 913–925.

Michalowski, R. and Mroz, Z. (1978). Associated and non-associated sliding rules in contact friction problems. *Arch. Mech.* **30**, 259–276.

Plesha, M. E., Ballarini, R. and Parulekar, A. (1989). *ASCE J. Engng Mech.* **115**, 2649–2668.

Qiu, X., Plesha, M. E. and Meyer, D. W. (1990). Stiffness matrix integration rules for contact-friction finite elements. *Comp. Meth. Appl. Mech. Engng* **93**, 385–399.

Steif, P. S. (1988). A simple model for the compressive failure of weakly bonded, fiber-reinforced composites. *J. Comp. Mater.* **22**, 818–828.

Thouless, M. D., Sbaizero, O., Sigl, L. S. and Evans, A. G. (1989). Effect of interfacial mechanical properties on pullout in a SiC-fiber-reinforced lithium aluminum silicate glass-ceramic. *J. Am. Ceram. Soc.* **72**, 525–532.

APPENDIX A

The formulation first assumes an additive decomposition of the incremental displacement jump, similar to that found in small-displacement gradient plasticity,

$$[\![\dot{\mathbf{u}}]\!] = [\![\dot{\mathbf{u}}]\!]^e + [\![\dot{\mathbf{u}}]\!]^s, \tag{A1}$$

where the superscripts e and s denote elastic and slip, respectively. Also, a linear relation between the traction increment and the elastic (penalized) part of the incremental displacement jump is assumed,

$$\dot{\mathbf{t}} = \mathbf{E}^e[\![\dot{\mathbf{u}}]\!]^e, \tag{A2}$$

where $\mathbf{E}^e$ is a diagonal matrix of penalty numbers which in the limit as $\mathbf{E}^e \to \infty$ would provide for full compatibility without slipping or interpenetration along the interface.

A final postulate is made concerning the directional nature of the slip,

$$[\![\dot{\mathbf{u}}]\!]^{\mathrm{cp}} = \begin{cases} \mathbf{0} & F < 0 \quad \text{or} \quad \dot{F} < 0, \\ \Lambda \dfrac{\partial H}{\partial \mathbf{t}} & F = 0 \quad \text{and} \quad \dot{F} = 0, \end{cases} \tag{A3}$$

where Λ is a parameter with the units of displacement rate, H is the slip potential, and F is the slip function, which in the case of three-dimensional Coulomb friction are [see Michalowski and Mroz (1978) and Curnier (1984)]:

$$F = \sqrt{t_{t1}^2 + t_{t2}^2} + \mu t_n, \quad H = \sqrt{t_{t1}^2 + t_{t2}^2}, \tag{A4}$$

where t_{t1} and t_{t2} are two orthogonal tractions that are tangential to the interface [Fig. 3(a)].

For the case of $F = 0$ and $\dot{F} = 0$, the traction increment can be written as

$$\dot{\mathbf{t}} = \hat{\mathbf{E}}[\![\dot{\mathbf{u}}]\!], \qquad \text{where} \quad \hat{\mathbf{E}} = \mathbf{E}^{\mathrm{e}} \left[\mathbf{I} - \frac{\dfrac{\partial H}{\partial \mathbf{t}} \dfrac{\partial^{\mathrm{T}} F}{\partial \mathbf{t}} \mathbf{E}^{\mathrm{e}}}{\dfrac{\partial^{\mathrm{T}} F}{\partial \mathbf{t}} \mathbf{E}^{\mathrm{e}} \dfrac{\partial H}{\partial \mathbf{t}}} \right]. \tag{A5}$$

The full constitutive law can therefore be stated by combining (13), (A.2) and (A5):

$$\dot{\mathbf{t}} = \mathbf{E}^{\mathrm{cp}}[\![\dot{\mathbf{u}}]\!], \qquad \text{where} \quad \mathbf{E}^{\mathrm{cp}} = \begin{cases} \mathbf{E}^{\mathrm{e}}, & [\![\mathbf{u}]\!] \cdot \mathbf{n} > 0; F < 0 \text{ or } \dot{F} < 0 \\ \hat{\mathbf{E}}, & [\![\mathbf{u}]\!] \cdot \mathbf{n} > 0; F = 0 \text{ and } \dot{F} = 0 \\ \mathbf{0}, & [\![\mathbf{u}]\!] \cdot \mathbf{n} \leq 0, \end{cases} \tag{A5}$$

where the total displacement jump $[\![\mathbf{u}]\!]$ is the integral of the incremental displacement jumps over the time history.

APPENDIX B

Equation (14) can be rewritten by considering the weak form for each of the continuum bodies and the interfaces for some finite thickness (see Fig. 2), integrating with respect to time, and after which summing over all bodies and taking the limit as the interface thickness approaches zero,

$$\begin{gathered} \dot{\mathbf{u}} \in \mathbf{U}; \quad a(\mathbf{w}, \dot{\mathbf{u}}) = \dot{F}^{\mathrm{ext}} + \dot{F}^{\mathrm{cp}} - \dot{a}(\mathbf{w}, \mathbf{t}, \dot{\mathbf{u}}) \quad \forall \mathbf{w} \in \mathbf{W} \\ a(\mathbf{w}, \mathbf{u}) = G \sum_{i=1}^{n} \int_{\Omega_i} \nabla \mathbf{w} : (\nabla \mathbf{u} + \nabla \mathbf{u}^{\mathrm{T}}) \, \mathrm{d}V + (K - \tfrac{2}{3}G) \sum_{i=1}^{n} \int_{\Omega_i} \mathrm{tr}\,(\nabla \mathbf{w})\, \mathrm{tr}\,(\nabla \mathbf{u}) \, \mathrm{d}V \\ \dot{a}(\mathbf{w}, \mathbf{t}, \dot{\mathbf{u}}) = \sum_{i=1}^{n} \sum_{j=i+1}^{n} \int_{\Omega_i \cap \Omega_j} [\![\mathbf{w}]\!] \cdot \mathbf{E}^{\mathrm{cp}}(t) \circ [\![\dot{\mathbf{u}}]\!] \, \mathrm{d}S \\ \dot{F}^{\mathrm{ext}} = \sum_{i=1}^{n} \int_{\Omega_i} \mathbf{w} \cdot \dot{\mathbf{f}} \, \mathrm{d}V + \sum_{i=1}^{n} \int_{\Gamma_\sigma \cap \Omega_i} \mathbf{w} \cdot \dot{\mathbf{h}} \, \mathrm{d}S \\ \dot{F}^{\mathrm{cp}} = \sum_{i=1}^{n} \int_{\Omega_i} \frac{\lambda}{\bar{s}} \left[\frac{\bar{s}}{2G} \right]^{\mathrm{cp}} \nabla \mathbf{w} : S \, \mathrm{d}V \\ \mathbf{W} = \{ \mathbf{w} \in \mathbf{H}^1 \mid \mathbf{w} = 0 \text{ on } \Gamma_v \} \\ \mathbf{U} = \{ \dot{\mathbf{u}} \in \mathbf{H}^1 \mid \dot{\mathbf{u}} = \dot{\mathbf{g}} \text{ on } \Gamma_v \} \end{gathered} \tag{B1}$$

where the impenetrability condition was dropped since the constitutive law is enforced using a penalty method, and the set of velocity functions $\dot{\mathbf{u}}$, have been extended to the set of functions whose first derivatives are contained within a Sobolov normed space (i.e. square integrable derivatives). For the notation, the jump in the weighting functions $\mathbf{w}$ is defined as $[\![\mathbf{w}]\!] = \mathbf{w}^{\prime} - \mathbf{w}^{\prime\prime}$ and the traction is defined as $\mathbf{t} = \mathbf{T} \circ \mathbf{n}^{\prime}$.

An isoparametric finite element formulation using a Bubnov–Galerkin approach, allows (B.1) to be written as

$$[\mathbf{K} + \mathbf{K}^{\mathrm{cp}}(t_m, t_{m+1})] \Delta \mathbf{d} = \mathbf{F} - \mathbf{F}^{\mathrm{int}} + \int_0^{t_n} \dot{\mathbf{F}}^{\mathrm{cp}}(\tau) \, \mathrm{d}\tau, \tag{B2}$$

with,

$$\begin{gathered} \mathbf{K} = \int_{-1}^{1} \int_{-1}^{1} \left\{ 2G\mathbf{B}^{\mathrm{T}}\mathbf{B} + \left(K - \frac{2G}{3} \right) \hat{\mathbf{B}}^{\mathrm{T}} \hat{\mathbf{B}} \right\} J \, \mathrm{d}V, \\ \mathbf{K}^{\mathrm{cp}}(t_m, t_{m+1}) = \int_{-1}^{1} \mathbf{M}^{\mathrm{T}} \{ \theta \mathbf{E}^{\mathrm{cp}}(t_m) + (1-\theta) \mathbf{E}^{\mathrm{cp}}(t_{m+1}) \} \mathbf{M} J \, \mathrm{d}S_0, \\ \mathbf{F} = \int_{-1}^{1} \int_{-1}^{1} \mathbf{N}^{\mathrm{T}} \mathbf{f} J \, \mathrm{d}V_0 + \int_{-1}^{1} \mathbf{N}^{\mathrm{T}} \mathbf{h} J \, \mathrm{d}S_0 - \int_{-1}^{1} \int_{-1}^{1} \left\{ 2G\mathbf{B}_g^{\mathrm{T}} \mathbf{B}_g + \left(K - \frac{2G}{3} \right) \hat{\mathbf{B}}_g^{\mathrm{T}} \hat{\mathbf{B}}_g \right\} \Delta g J \, \mathrm{d}V_0 \\ - \int_{-1}^{1} \mathbf{M}_g^{\mathrm{T}} \{ \theta \mathbf{E}^{\mathrm{cp}}(t_m) + (1-\theta) \mathbf{E}^{\mathrm{cp}}(t_{m+1}) \} \Delta g J \, \mathrm{d}S_0. \end{gathered} \tag{B3}$$

$$\mathbf{F}^{\text{int}} = \int_{-1}^{1}\int_{-1}^{1}\left\{2G\mathbf{B}^{\mathrm{T}}\mathbf{B} + \left(K - \frac{2G}{3}\right)\hat{\mathbf{B}}^{\mathrm{T}}\hat{\mathbf{B}}\right\} d(t_m) J \, \mathrm{d}V_0 + \int_{-1}^{1} \mathbf{M}^{\mathrm{T}}\mathbf{t}(t_m)\mathbf{J} \, \mathrm{d}S_0,$$

$$\dot{\mathbf{F}}(t)^{\alpha} = \int_{-1}^{1}\int_{-1}^{1} \frac{\dot{\lambda}}{\bar{s}(t)}\left[\frac{\bar{s}(t)}{2G}\right]^{\alpha} \hat{\mathbf{B}}^{\mathrm{T}}\mathbf{s}(t) J \, \mathrm{d}V_0,$$

where the deviatoric stress vector (s), the shape function operators ($\mathbf{B}$ and $\mathbf{M}$), and the Jacobian determinants ($\mathbf{J}$) are defined in Meyer *et al.* (1992b). The form of the stiffness matrix is given in Fig. 4 where the full length rows result from the common degrees of freedom given in eqns (1) and (2).